J Mol Model (2014) 20:2466
DOI 10.1007/s00894-014-2466-3

ORIGINAL PAPER

Reaction of Np atom with H_2O in the gas phase: reaction mechanisms and ab initio molecular dynamics study

Peng Li · Wenxia Niu · Tao Gao · Hongyan Wang

Received: 26 April 2014 / Accepted: 14 September 2014 / Published online: 7 October 2014

Abstract The gas-phase reaction of an Np atom with H_2O was investigated using density functional theory and ab initio molecular dynamics. The reaction mechanisms and the corresponding potential energy profiles for different possible spin states were analyzed. Three reaction channels were found in the mechanism study: the isomerization channel, the H_2 elimination channel, and the H atom elimination channel. The latter two were observed in the dynamics simulation. It was found that the branching ratio of the title reaction depends on the initial kinetic energy along the transition vector. Product energy distributions for the reaction were evaluated by performing direct classical trajectory calculations on the lowest sextet potential energy surface. The results indicate that most of the available energy appears as the translational energy of the products. The overall results indicate that the H_2 elimination channel with low kinetic energy is thermodynamically favored but competes with the H atom elimination channel with higher kinetic energy.

Keywords Hydrolysis reaction · DFT · Reaction mechanisms · Bonding analysis · Ab initio molecular dynamics · Product energy distributions

P. Li · T. Gao (✉)
Institute of Atomic and Molecular Physics, Sichuan University, Chengdu 610065, China
e-mail: gaotao@scu.edu.cn

W. Niu
College of Physical Science and Technology, Sichuan University, Chengdu 610065, China

H. Wang
School of Physical Science and Technology, Southwest Jiaotong University, Chengdu 610031, China

Introduction

Over the last few decades, the reactions of actinide with small molecules in the gas phase have attracted significant attention; theoretical and experimental investigations of these systems have been performed because of their central importance in actinide chemistry [1–12]. One of the main objectives of such studies has been to analyze their characteristic electronic structures and chemical properties. In particular, the hydrolysis chemistry of the actinides has a major influence on the corrosive effect of steam, and on nuclear fuel reprocessing cycles. Another topic of interest in these investigations is the activation of prototypical chemical bonds, leading to a fundamental understanding of the corresponding reaction mechanisms, kinetics, and thermodynamics.

Neptunium, which is commonly produced by irradiating uranium with neutrons in nuclear reactors and is generated as a by-product in conventional nuclear power reactors, is a reactive metal. When exposed to air, neptunium oxidizes quickly. This corrosion reaction proceeds more rapidly as the temperature increases. The gas-phase chemistry of monopositive and dipositive neptunium has been studied by Gibson and collaborators using Fourier transform ion cyclotron resonance mass spectrometry (FTICR-MS) experiments [8, 11]. The reaction products and reaction efficiencies of Np^+ and Np^{2+} + H_2O were determined in their research. However, to the best of our knowledge, experimental data on the direct reaction of an Np atom with H_2O are scarce, and there are also no theoretical studies on the geometries or electronic structures of the reaction products. Theoretical calculations are of fundamental importance in attempts to deepen our knowledge of the reaction mechanism. A systematic investigation of the reactivity of an Np atom with H_2O should provide greater insight into this chemistry.

Ab initio quantum chemical and density functional (DFT) methods have proven to be very helpful tools for improving our understanding of *f*-block element chemistry. Theoretical studies can be especially valuable in providing additional detailed information about reaction mechanisms and dynamics [13, 14]. Uranium is one of the most well-studied actinides, and its reactions with H_2O were investigated using DFT [12]. The reaction mechanisms for $U+H_2O$ are illustrated by the following equations:

$$U + H_2O \rightarrow HU(OH) \rightarrow H_2UO$$
$$U + H_2O \rightarrow HU(OH) \rightarrow UO + H_2 .$$

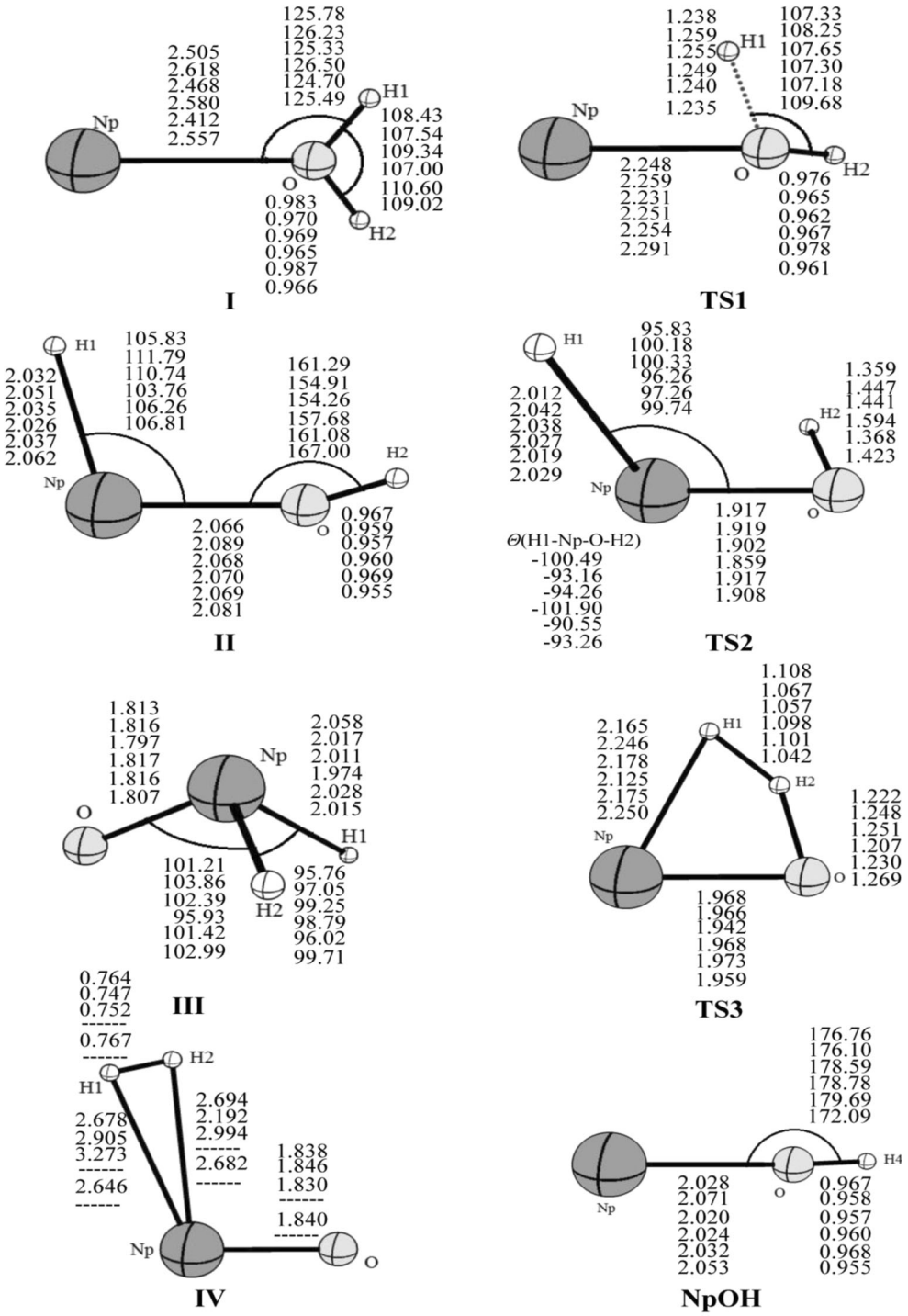

Fig. 1 Structures and selected geometric parameters of stationary points on the $NpOH_2$ potential energy surface optimized at the PW91/SDD, B3LYP/SDD, PBE0/SDD, MP2/SDD, BP86/SDD, and BMK/SDD levels of theory (from *top* to *bottom rows*, respectively). Complex III ($ONpH_2$) was predicted to have a pyramidal structure. Θ(H1–Np-O-H2) is the dihedral angle of TS2. Bond distances are in Å and angles are in degrees

According to experiments performed by Gibson and collaborators [8], the reactions of U^+ and Np^+ with H_2O have similar reaction efficiencies k/k_{ADO} [rate constants (k) and average dipole orientation collisional rate constants (k_{ADO})] and reaction products (U^+: k/k_{ADO}=0.13, UO^+ and UOH^+ are produced; U^+: k/k_{ADO}=0.10, NpO^+ and $NpOH^+$ are produced). Therefore, we thiought that previous experimental and theoretical calculations of the reaction of a U atom with water could provide us with some inspiration when investigating the reaction of $Np+H_2O$.

The work reported in the present paper focused on the dynamics of the gas-phase reaction of an Np atom with H_2O. A series of calculation methods were used to describe structural parameters and mechanisms as accurately as possible. The dynamics of the reaction were simulated by means of ab initio molecular classical trajectory calculations. Product energy distributions (PEDs) for the reaction were evaluated on the lowest potential energy surface.

Computational details

Geometry optimization and calculations of harmonic vibrational frequencies on the potential energy surfaces of all possible spin states were computed at different levels of density functional theory (DFT). The PW91PW91 [15, 16], B3LYP [17, 18], PBE0 [19], MP2 [20], BP86 [21, 22], and BMK [23] functionals were used. The small-core Stuttgart relativistic effective core potential (SDD) [24] for the Np atom was employed in all calculations. This relativistic effective core potential (RECP) replaces the 60 electrons in inner shells 1–4, leaving the $n\geq5$ shell (5*s*, 5*p*, 5*d*, 5*f*, 6*s*, 6*p*, 6*d*, and 7*s*) as valence electrons. The 6-311++G(d,p) basis sets of Pople and

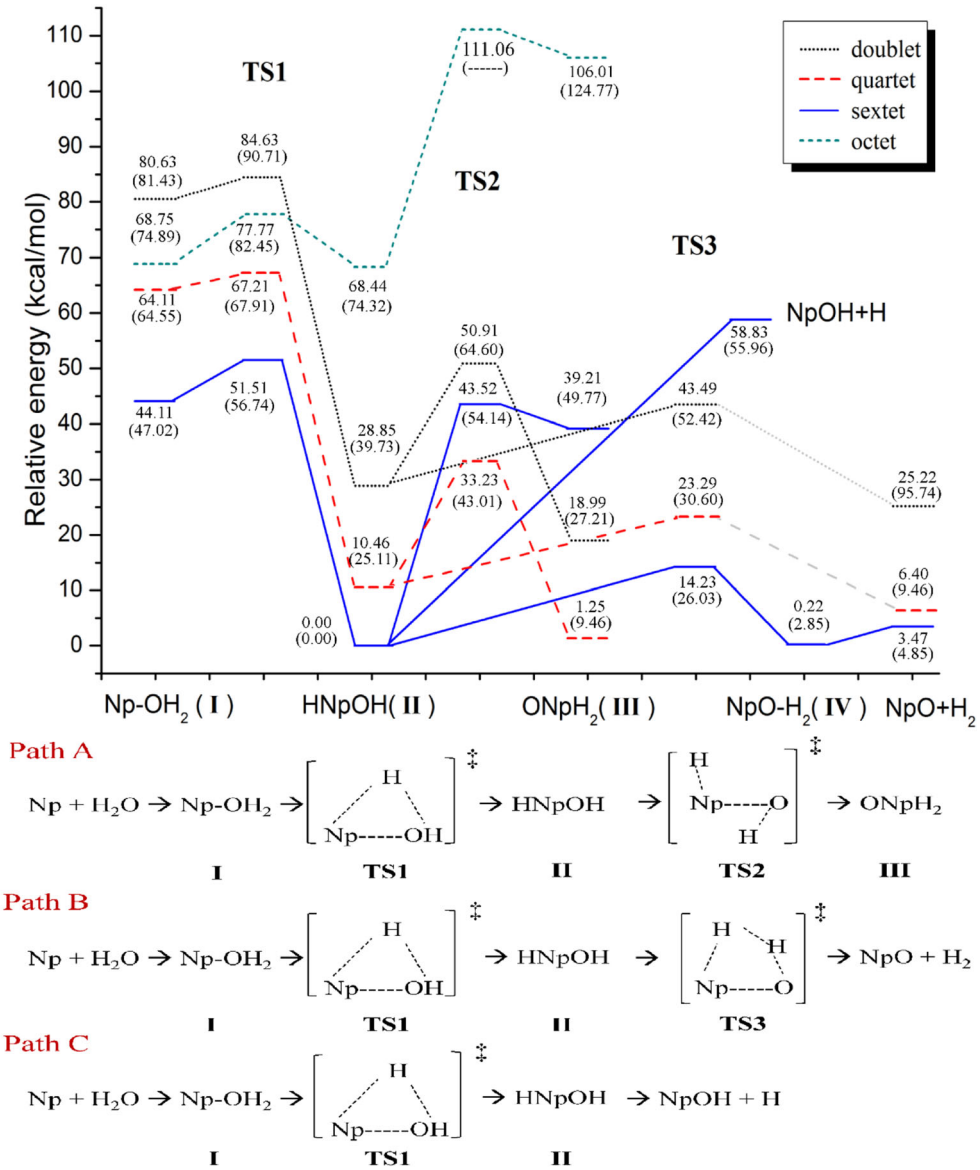

Fig. 2 Potential energy profile for the isomerization and dissociation of $NpOH_2$, as computed at the PW91/SDD and B3LYP/SDD (*in parentheses*) levels of theory

Table 1 Relative energies (kcal/mol) of the stationary points on the $NpOH_2$ potential energy surface

	I(6)	TS1(6)	II(6)	TS2(4)	III(4)	TS3(6)	IV(6)	$NpO+H_2$	NpOH+H
PW91 [a]	44.11	51.51	0.00	33.23	1.25	14.23	0.22	3.47	58.83
B3LYP [a]	47.02	56.74	0.00	43.01	9.46	26.03	2.85	4.85	55.96
PBE0 [a]	56.80	59.67	0.00	43.67	10.46	20.20	4.41	7.60	57.14
BP86 [a]	51.45	62.09	0.00	32.70	0.63	15.44	−0.15	16.85	60.22
BMK[a]	51.98	59.99	0.00	49.74	3.42	32.52	*f*	9.41	49.36
MP2 [a]	51.78	64.00	0.00	50.86	−15.82	17.23	*f*	20.61	86.19
PW91-SR [b]	37.16	49.17	0.00	24.26	−2.53	8.38	−5.75	4.34	58.26
PW91-SO [c]	53.50	62.85	0.00	30.62	−3.78	13.70	−2.89	−1.09	63.56
CCSD(T) [d]	64.01	76.79	0.00	50.64	10.20	45.82	*f*	32.33	101.54
CCSD(T) [e]	41.39	79.77	0.00	25.19	15.73	42.03	5.28	1.44	35.23
$<S^2>$[g]	8.763	8.768	8.761	4.237	3.801	8.765	8.767		

[a] SDD for Np and 6-311++G(d,p) for H and O atoms. [b] Frozen-core TZP for Np and TZ2P for H and N atoms, PW91/ ZORA-SR. [c] Frozen-core TZP for Np and TZ2P for H and N atoms, singlet point PW91/ZORA-SO results. [d] Single-point energy on the MP2/SDD optimized geometries. [e] Single-point energy on the PW91/SDD optimized geometries. [f] Cannot be located. [g] Expectation value of S^2 at the PW91/SDD level of theory

co-workers were employed for the O and H atoms [25]. These calculations were carried out using the Gaussian 09 suite of programs [26]. This computational methodology was successfully applied in a previous mechanism and molecular dynamics study of gas-phase actinide chemistry [2–5, 7, 14]. We carefully checked that the transition state calculated on each potential energy surface had only one imaginary frequency and that its vibrational mode corresponded to the correct movement of the atoms involved. Also, this frequency correctly connected reactants and products, as proven by intrinsic reaction coordinate (IRC) calculations. All relative energies was corrected for the zero-point vibrational energy (ZPVE). We checked the$<S^2>$values to make sure that spin contamination was not serious in most of the cases. In addition, single-point single-reference coupled cluster calculations including single, double, and perturbative triple configurations (CCSD(T)) [27, 28] were performed on the MP2/SDD and PW91/SDD optimized geometries. Bonding analysis was performed within the natural bond orbital (NBO) scheme [29, 30] in order to gain insight into the evolution of the chemical bonds in the reaction.

The zeroth-order regular approximation (ZORA) [31, 32] was applied and scalar relativistic (SR) effects were accounted for using the ADF2013.01 package [33]. The PW91 functional and the type TZP basis set [34] were employed for the Np atom, and the TZ2P basis set [34] for H and O atoms. The frozen-core approach was implemented to describe the inner electrons of Np and O. For the Np atom, all electrons up to the 5*d* orbitals were considered frozen; for the O atom, 1*s* was frozen. In addition, single-point spin-orbit ZORA-SO calculations were performed on the optimized geometries obtained at the PW91/ZORA-SR level of theory to take into account the spin–orbit effect.

Direct classical trajectory calculations were computed at the PW91/SDD level of theory, which was used because it was considered to be the best compromise between computational cost and accuracy. A microcanonical ensemble of initial states was constructed using normal mode sampling [35]. In our calculations, Born–Oppenheimer molecular dynamics (BOMD) [36] was employed as implemented in the Gaussian 09 package. This method uses a fifth-order polynomial fitted to the energy, gradient, and Hessian at each time step [37], and generating the correction step enables the

Table 2 Vibrational frequencies (cm^{-1}) for the transition states calculated at the PW91/SDD, B3LYP/SDD, and PBE0/SDD levels

TS1			TS2			TS3		
PW91	B3LYP	PBE0	PW91	B3LYP	PBE0	PW91	B3LYP	PBE0
1164.89*i*	1311.74*i*	1372.50*i*	1279.19*i*	1239.84*i*	1186.52*i*	1188.24*i*	1481.87*i*	1330.26*i*
249.31	163.36	195.83	373.16	341.81	327.98	729.73	736.37	779.36
491.82	412.79	435.68	409.71	392.31	376.03	874.25	833.97	893.38
777.12	712.85	720.26	783.15	757.20	777.14	1157.91	1243.22	1216.95
2149.07	1341.61	1389.45	1354.78	1277.04	1306.49	1452.77	1503.48	1565.93
3671.45	3809.22	3874.53	1411.65	1361.81	1386.74	1814.44	1834.08	1859.24

step size to be increased by a factor of 10 or more over previous implementations. The Hessians were updated for five steps before being recalculated analytically. A total of 400 trajectories (200 trajectories for each reaction channel) were initiated at the TS toward the products in our calculations. The initial conditions were similar to those chosen by Schlegel [7]. The rotation sampling temperature was 300 K. The trajectories were terminated when the centers of mass of the fragments became separated by >12 bohr. The energy and angular momentum were conserved to better than 10^{-5} hartree and $10^{-8}\hbar$, respectively.

Table 3 Results of direct trajectory calculations for the reaction with 20 kcal/mol of extra energy, carried out at the PW91/SDD level of theory[a]

Channel	Number of trajectories	Proportion (%)
$NpO+H_2$	200	97.09
NpOH+H	6	2.91
Sum	206	100

[a] The trajectories included for each path successfully dissociated in the simulations

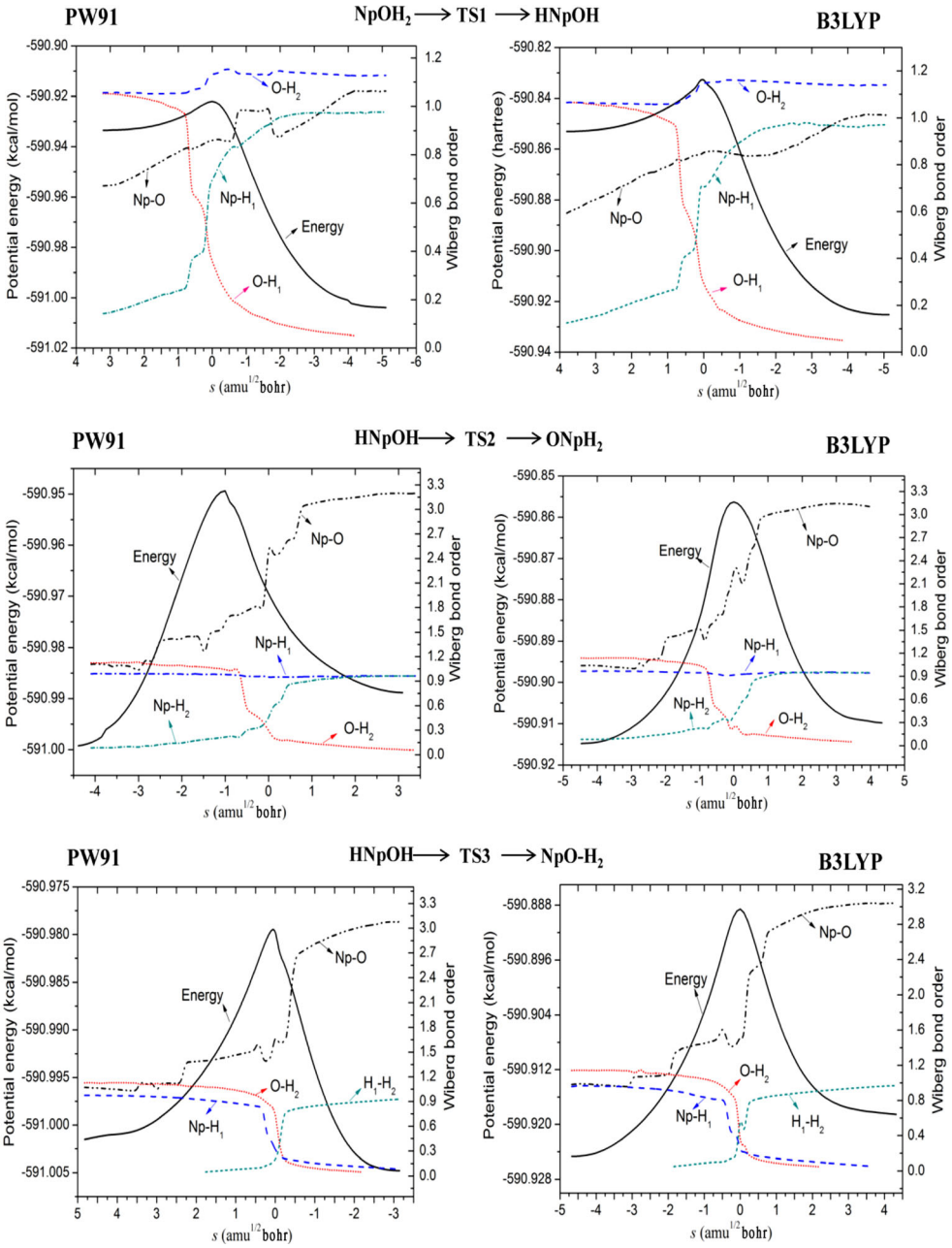

Fig. 3 Potential energy and Wiberg bond order along the intrinsic reaction coordinate *s*, as calculated at the PW91/SDD and B3LYP/SDD levels. *Black solid curves* are the energy and *dashed lines* are the Wiberg bond order (bond orders of<0.05 are not shown)

Table 4 Results of direct trajectory calculations for the reaction with 30 kcal/mol of extra energy, carried out at the PW91/SDD level of theory[a]

Channel	Number of trajectories	Proportion (%)
$NpO+H_2$	15	6.98
NpOH+H	200	93.02
Sum	215	100

[a] The trajectories included for each path successfully dissociated in the simulations

Results and discussion

Structure, energetics, and bonding analysis

The $NpOH_2$ and intermediate complexes, transition states, and products were optimized at different levels of theory. The corresponding geometric parameters are compared in Fig. 1 and show relatively little dependence on the level of theory. The relative energies of these stationary structures in the isomerization and dissociation of $NpOH_2$ at the PW91/SDD and B3LYP/SDD levels are depicted in Fig. 2. As shown in Fig. 2, three reaction channels were found: (1) a channel leading to rearrangement of the H_2NpO isomer (path A), (2) an H_2 elimination channel (the products are $NpO+H_2$; path B), and (3) an H atom elimination channel (the products are NpOH+H; path C). Our calculations confirm that the reaction of Np and H_2O has a similar mechanism to the reaction of U and water. Both the isomerization reaction channel and the H_2 elimination channel were determined for $U+H_2O$; the UOH+H channel was not observed [12].

Our results indicate that the sextet spin state remains as the ground state for the whole of path B, and it is proposed that this channel occurs by a similar mechanism to the insertion mechanism for the bare cations [2–4]. In path A, the reaction starts in the sextet reactant ground state, and intersystem crossing to the quartet spin state occurs after the system forms complex II (HNpOH). The rest of the isomerization reaction evolves along the quartet spin surface. In this process, therefore, the spin crossing occurs before the system has surmounted TS2. In path C, the product NpOH can be formed by direct cleavage of the H–Np bond in the hydroxy intermediate (HNpOH). Scan calculations performed for various H–Np bond lengths indicate that the H–Np bond-breaking process is an intrinsically barrierless transition. This notion is also supported by BOMD simulations.

We also considered the possible formation of HNp+OH and the separation of charge into $HNp^+ + OH^-$. However, neither of these cases are energetically favored. Their relative energies with respect to HNpOH were calculated to be

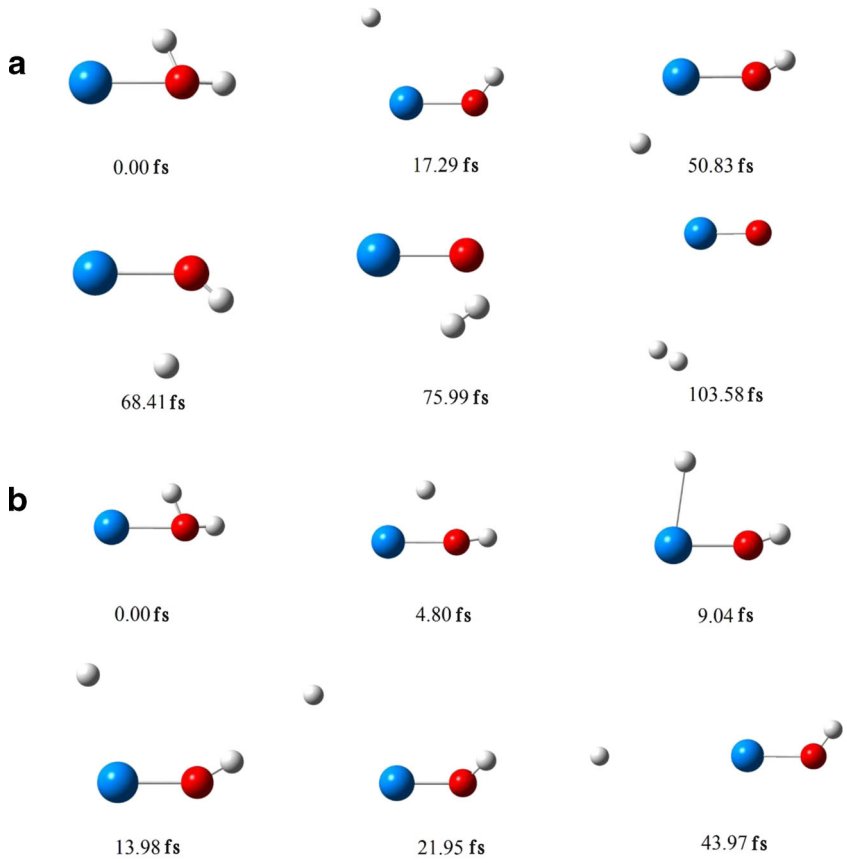

Fig. 4a–b Snapshots of typical trajectories from the MD simulations: **a** $NpOH_2 \rightarrow NpO+H_2$; **b** $NpOH_2 \rightarrow NpOH+H$

133.70 kcal/mol and 567.08 kcal/mol at the PW91/SDD level of theory, respectively.

As is well known, some DFT methods accurately predict energies, but the results they provide can be sensitive to the functional used. Therefore, different DFT functionals were employed to investigate the potential energy surfaces (PESs). The relative energies of selected stationary points on the PESs are collected in Table 1. These methods included pure generalized gradient approximation (GGA) functionals, a hybrid functional, second-order Møller–Plesset perturbation theory, and coupled-cluster calculations with effective core potentials (ECP)—a range of methods that permitted a broad survey of the structures associated with and the energetics of the reaction. The vibrational frequencies for the transition states calculated at the PW91/SDD, B3LYP/SDD, and PBE0/SDD levels are listed in Table 2.

When there are no experimentally determined structural parameters and energy values for a system, it is important to calculate the system using different functionals to see if they give consistent results [38]. As can be seen in Table 1, the DFT and MP2 calculations, especially those performed using the PW91/SDD and B3LYP/SDD methods, give consistent relative energies. On the other hand, the BMK/SDD and BP86 methods appear to be inappropriate for complex IV. Although the MP2 method is sometimes still considered to be more reliable than DFT, we found that it did not perform as well for TS2 and complex III. Single-point CCSD(T)/SDD calculations on the MP2/SDD- and PW91/SDD-optimized geometries were also performed. The PW91/SDD calculations are in reasonable agreement with single-point CCSD(T) on PW91/SDD-optimized geometries, especially for dissociation reactions, indicating that PW91/SDD should provide trusted results. On the contrary, single-point CCSD(T) calculations on MP2/SDD-optimized geometries significantly overestimate the exothermicity of paths B and C. Turning our attention to the vibrational constants of the transition states, we note that hybrid DFT (B3LYP and PBE0) systematically gives higher values than PW91 for TS1 and TS3, as shown in Table 2. This conclusion is also supported by DFT benchmarking studies of the thermochemistry of the oxofluorides of uranium by Schreckenbach and collaborators [15]. Therefore, PW91/SDD was chosen for the direct trajectory calculations as it is a practical method that gives satisfactory results.

Spin–orbit effects were evaluated using the ZORA-SO method. ZORA-SO calculations are an efficient way to take into account the spin–orbit effect, particularly when there is an

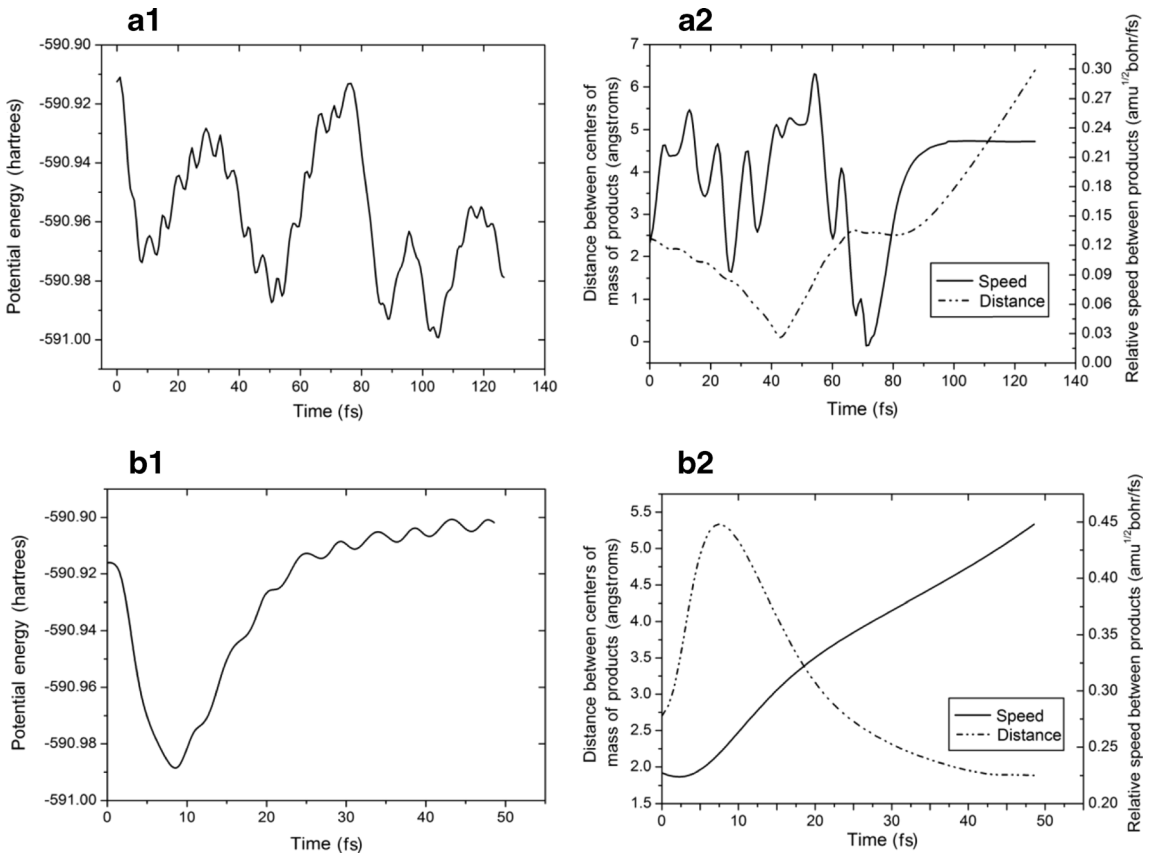

Fig. 5 Changes in the potential energy and the relative speed and distance between products over simulation time: **a1** time evolution of the potential energy for $NpOH_2 \rightarrow NpO+H_2$; **a2** relative speed and distance between products for $NpOH_2 \rightarrow NpO+H_2$; **b1** time evolution of the potential energy for $NpOH_2 \rightarrow NpOH+H$; **b2** relative speed and distance between products for $NpOH_2 \rightarrow NpOH+H$

actinide complex among the products of the reaction. As can be seen in Table 2, the spin–orbit ZORA method also gave consistent relative energies. The PW91/ZORA-SO calculations were consistent with those afforded by PW91/SDD, which means that the spin–orbit corrections have little effect on these computed complexes. This conclusion is supported by experimental data [39, 40]. Experience with actinide molecular systems has shown that the major spin–orbit effects occur for the free actinide atoms or cations, whereas rather small corrections are found for molecular complexes. Theoretical results for similar systems also point to this behavior. A study of the activation of water by U cations and oxides showed that spin–orbit corrections have little effect on the activation barriers of the transition states [1, 2]: in most cases, the corrections were found to be less than 10 kJ/mol.

Bonding analysis

In order to gain a deeper understanding of the reaction mechanisms, we investigated the evolution of the bonds along the pathways using natural bond orbital (NBO) analysis. The potential energy and Wiberg bond order [41] along the intrinsic reaction coordinate *s* calculated at the PW91/SDD and B3LYP/SDD levels are detailed in Fig. 3. Noting that the hybrid functional predicts that structures are more ionic and less covalent than the pure GGA does for compounds containing actinide elements [15], we chose these two complementary methods in order to achieve a more credible bond analysis. From Fig. 3, we can clearly see that, as the reaction proceeds, the bond orders of the breaking bonds gradually decrease to zero, while those of the new bonds gradually increased. Furthermore, the transition state is positioned near to the crossing point of these two sets of bond orders (the forming bonds and the breaking bonds). Figure 3 shows that the initial cleavage of the O–H_1 bond and the initial formation of the Np–H_1 bond takes place at the $NpOH_2 \rightarrow TS1 \rightarrow$ HNpOH stage of the reaction. During this process, the interaction between Np and O gradually strengthens. There is a significant increase in the bond order of Np–O at the $HNpOH \rightarrow TS2 \rightarrow H_2NpO$ stage. Bond order analysis provides a clear description of the formation of the second Np–H_2 covalent bond, as shown by the increase in the bond order of Np–H_2. By the end of this stage, the bond orders of Np–H_1 and Np–H_2 bond gradually become equal. In the isomerization reaction, a pyramidal structure is predicted for the product $ONpH_2$, in which the two Np–H bonds are almost symmetrical. The second O–H bond is completely broken, as evidenced by the gradual decrease in the bond order of the O–H_2 bond to

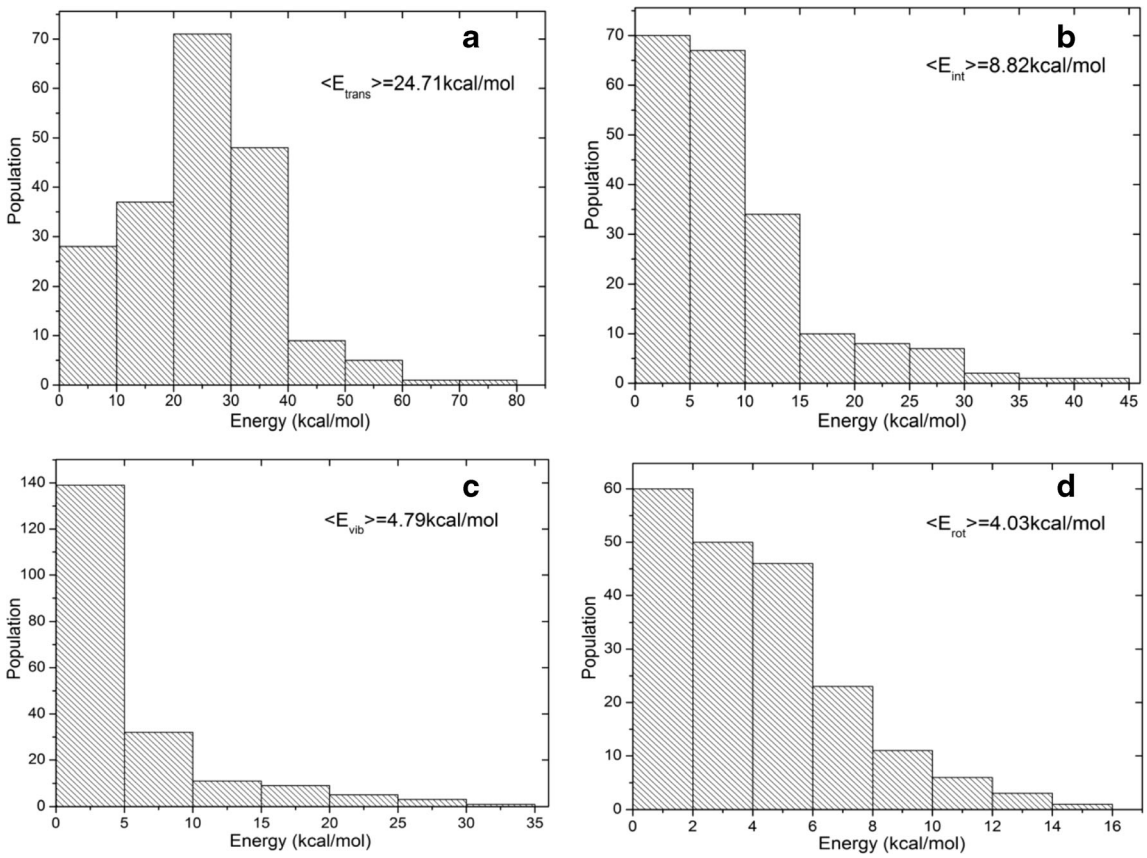

Fig. 6a–d Product energy distributions for path B: **a** relative translational energy between H_2 and NpO; **b** internal energy of NpO; **c** vibrational energy of NpO; **d** rotational energy of NpO

zero. In the H_2 elimination channel, HNpOH→TS3→ONp-H_2, the bond order of the reaction intermediate shows that the H_1–Np and O-H_2 covalent bonds are completely broken in this step, leading to the formation of H_1–H_2. The bond-order description for H_1–H_2 shows that it is comparable to the corresponding values for the free H_2 molecule.

Dynamics

To obtain a detailed description of the title reaction, the molecular dynamics (MD) of the Np+H_2O reaction were simulated using classical trajectory calculations. The preceding discussion of the energetics and frequencies showed that the PW91/SDD level of theory is suitable and practical for simulating the dynamics of the dissociation of $NpOH_2$. In the present calculations, 200 reactive trajectories for path B and 200 reactive trajectories for path C were carried out. It must be mentioned that each of these 200 trajectories for each path dissociated in the simulation. In fact, we actually calculated around 410 trajectories for each path, but 51.3 % of those trajectories did not dissociate in the simulation time (500 fs); they remained in the complex II (HNpOH) region. This may be because complex II is a deep well on the potential energy surface, so longer simulation times are needed for these trajectories.

Trajectories were initiated in the first transition state, with 20 kcal/mol and 30 kcal/mol extra energy distributed microcanonically among the vibration modes and to the transition vector, respectively. This initial energy was used to ensure that most of the trajectories reached the products in a timely fashion. When the barrier was greater than 5–10 kcal/mol, very few trajectories reached the products. In such cases, it is common practice to calculate trajectories from the transition state. As mentioned above, about 210 reactive trajectories for each path did not dissociate within the simulation time because the energy was not conserved or the integration failed. The trajectories were computationally intensive: in total, our calculations used more than 2 years of CPU time. Therefore, a good balance between the level of theory used for trajectory calculations and the overall accuracy of the results must be maintained.

Our calculations reveal that the branching ratio for the two channels varied as the initial kinetic energy along the transition vector changed. As shown by the results of direct trajectory calculations for the reaction listed in Tables 3 and 4, the NpO+H_2 channel is favored at low extra energy and the NpOH+H channel competes at higher extra energy. We did not observe trajectories corresponding to the isomerization reaction from HNpOH to H_2NpO within the simulation time.

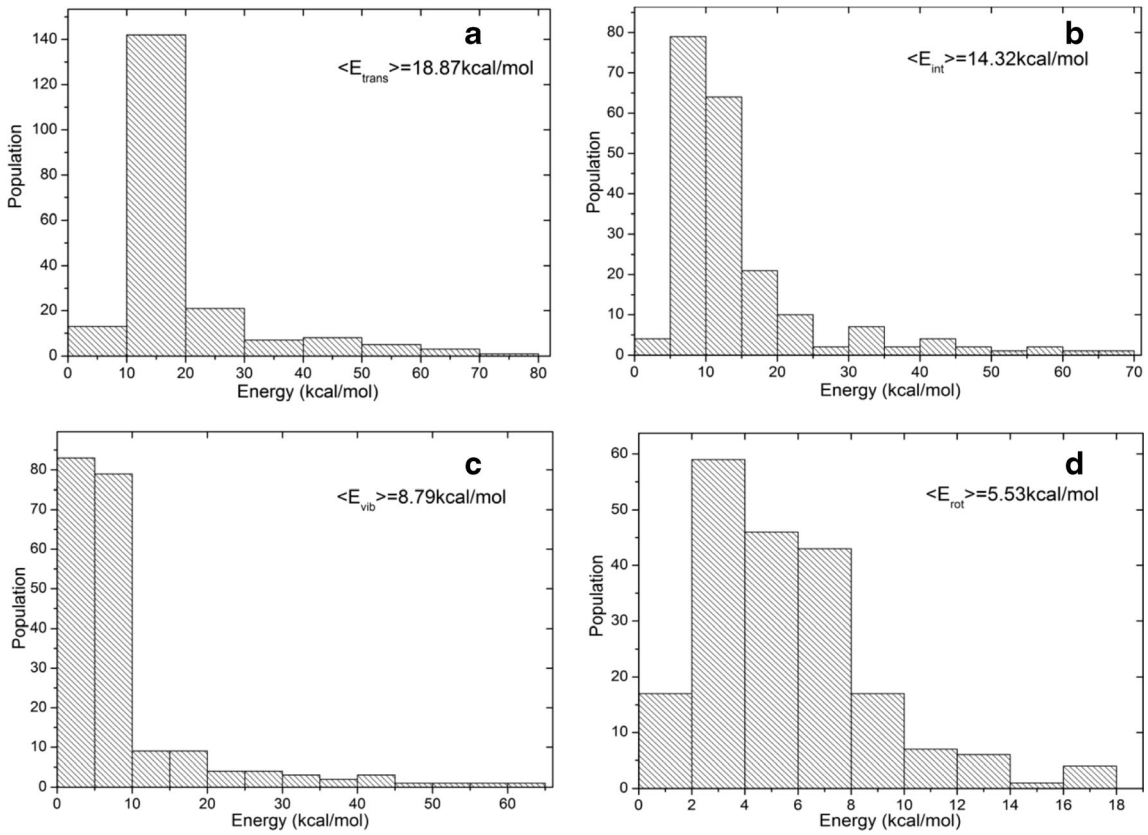

Fig. 7a–d Product energy distributions for path C: **a** relative translational energy between H and NpOH; **b** internal energy of NpOH; **c** vibrational energy of NpOH; **d** rotational energy of NpOH

Typical snapshots along the BOMD trajectory are presented in Fig. 4, and the corresponding time evolutions of the potential energy and the relative speed and distance between products are illustrated in Fig. 5. It is apparent that the HNpOH intermediate can easily be generated in both channels, and that it formed from TS1 at around 15 fs. Another obvious feature is that the NpOH+H channel is faster, since H atom elimination yields the HNpOH intermediate in this channel without passing through a transition state.

Statistics for the translational, vibrational, and rotational energies of the products allow detailed insight into the potential energy surface and illustrate which energy form is the most of the available energy transferred into [42]. The product energy distributions (PEDs) for the H_2 elimination channel and the H atom elimination channel are shown in Figs. 6 and 7, respectively. For the H_2 elimination channel, as shown in Fig. 6, the relative translational energies range from 0 to 80 kcal/mol with a peak at around 20–30 kcal/mol, and the average value is 24.71 kcal/mol. The internal energies of NpO range from 0 to 45 kcal/mol, with the peak occurring at around 0–5 kcal/mol. The vibrational energies of NpO are seen to range from 0 to 35 kcal/mol with a peak at around 0–5 kcal/mol. The rotational energies of NpO present a narrow distribution, ranging from 0 to 16 kcal/mol with an average value of 4.03 kcal/mol. The average available energy calculated by BOMD at the PW91/SDD level for the reaction was 33.53 kcal/mol. Average energies of 24.71 (73.6 %), 4.79 (14.2 %), and 4.03 (12.2 %) kcal/mol were partitioned into the relative translational energies and the vibrational and rotational energies of NpO, respectively. Therefore, most of the available energy was transferred into the translational energy of the products.

For the H atom elimination channel, as shown in Fig. 7, the average available energy is 33.16 kcal/mol. On average, 18.87 kcal/mol (56.9 %) of this available energy is transferred into the total translational energy of the products, 8.79 kcal/mol (26.5 %) goes into the vibrational energy of NpOH, and 5.53 kcal/mol (16.9 %) is directed into the rotational energy of NpOH. Upon comparing the H_2 elimination channel and H atom elimination channel, the following conclusions can be drawn: most of the available energy is funneled into the relative translational energies of the products, and the difference between the two channels is that the translational energy is reduced while the internal energy (vibrational+rotational energy) is increased in the H atomic elimination channel.

Conclusions

The present article describes an ab initio molecular dynamics study of, and provides detailed information on, the reaction of an Np atom with H_2O. Three reaction channels were found from reaction mechanism studies: an isomerization channel, an H_2 elimination channel, and an H atom elimination channel. The latter two reactions were observed to occur in the dynamics simulation. It is found that the branching ratio for the two channels varied as the initial kinetic energy along the transition vector was changed. Product energy distributions (PEDs) for the reaction were evaluated via direct classical trajectory calculations. The average available energy estimated at the PW91/SDD level for the H_2 elimination reaction was 33.53 kcal/mol, and on average 24.71 (73.6 %), 4.79 (14.2 %), and 4.03 (12.2 %) kcal/mol were partitioned into the relative translational energyies and the vibrational and rotational energies of NpO, respectively. For the H atom elimination reaction, 56.9 %, 26.5 %, and 16.9 % of the available energy (33.16 kcal/mol) were partitioned into the relative translational energies and the vibrational and rotational energies of NpOH, respectively. Overall, it is clear that most of the available energy is transferred into the relative translational energies of the products in both reaction channels.

Acknowledgments We are very grateful to Dr. Xiaofeng Tian and Dr. Sobereva for many helpful discussions. Computer time made available by the Center of High Performance Computing at the Physics Discipline of Sichuan University is gratefully acknowledged. We would like to thank the reviewers for their valuable suggestions for improving our paper.

References

1. Michelini MC, Russo N, Sicilia E (2006) Angew Chem Int Ed 45: 1095–1099
2. Michelini MC, Russo N, Sicilia E (2007) J Am Chem Soc 129:4229–4239
3. Alikhani ME, Michelini MC, Russo N, Sicilia E (2008) J Phys Chem A 112:12966–12974
4. Mazzone G, Michelini MC, Russo N, Sicilia E (2008) Inorg Chem 47:2083–2088
5. De Almeida KJ, Duarte HA (2009) Organometallics 28:3203–3211
6. De Almeida KJ, Duarte HA (2010) Organometallics 29:3735–3745
7. Zhou J, Schlegel HB (2010) J Phys Chem A 114:8613–8617
8. Santos M, Mar alo J, Pires de Matos A, Gibson JK, Haire RG (2002) J Phys Chem A 106:7190–7194
9. Jackson GP, King FL, Goeringer DE, Duckworth DC (2002) J Phys Chem A 106:7788–7794
10. Liang BY, Andrews L, Li J, Bursten BE (2002) J Am Chem Soc 124: 6723–6733
11. Gibson JK, Haire RG, Santos M, Mar alo J, Pires de Matos A (2005) J Phys Chem A 109:2768–2781
12. Liang BY, Hunt RD, Kushto GP, Andrews L, Li J, Bursten BE (2005) Inorg Chem 44:2159–2168
13. Koch W, Holthausen MC (2000) A chemist's guide to density functional theory. Wiley-VCH, New York
14. Shamov GA, Schreckenbach G, Vo TN (2007) Chem Eur J 13:4932–4947
15. Perdew JP, Chevary JA, Vosko SH, Jackson KA, Pederson MR, Singh DJ, Fiolhais C (1992) Phys Rev B 46:6671–6687
16. Perdew JP, Burke K, Wang Y (1996) Phys Rev B 54:16533–16539
17. Becke AD (1993) J Chem Phys 98:5648–5652
18. Lee C, Yang W, Parr RG (1988) Phys Rev B 37:785–789

19. Adamo C, Barone VT (1999) J Chem Phys 110:6158–6170
20. Møller C, Plesset MS (1934) Phys Rev 46:618–622
21. Perdew JP (1986) Phys Rev B 33:8822–8824
22. Becke AD (1988) Phys Rev A 38:3098–3100
23. Boese AD, Jan MLM (2004) J Chem Phys 121:3405–3416
24. Kuchle W, Dolg M, Stoll H, Preuss H (1994) J Chem Phys 100:7535–7542
25. Krishnan R, Binkley JS, Seeger R, Pople JA (1980) J Chem Phys 72:650–654
26. Frisch MJ, Trucks GW, Schlegel HB, Scuseria GE, Robb MA, Cheeseman JR, Scalmani G, Barone V, Mennucci B, Petersson GA et al. (2009) Gaussian 09, revision A.02. Gaussian, Inc., Wallingford
27. Raghavachari K, Trucks GW, Pople JA, Head-Gordon M (1989) Chem Phys Lett 157:479–483
28. Pople JA, Head-Gordon M, Raghavachari K (1987) J Chem Phys 87:5968–5975
29. Reed AE, Weinhold F (1985) J Chem Phys 83:1736–1740
30. Reed AE, Curtiss LA, Weinhold F (1988) Chem Rev 88:899–926
31. Evan L, Snijders JG, Bearends EJ (1996) J Chem Phys 105:6505–6516
32. Evan L, Baerends EJ, Snijders JG (1994) J Chem Phys 101:9783–9792
33. Te Velde G, Bickelhaupt FM, Baerends EJ, Fonseca Guerra C, Gisbergen SJA, Snijders JG, Ziegler T, Te Velde G, Bickelhaupt FM, Baerends EJ, Fonseca Guerra C, Gisbergen SJA, Snijders JG, Ziegler T (2001) J Comput Chem 22:931–967
34. Van Lenthe E, Baerends EJ (2003) J Comput Chem 24:1142–1156
35. Peslherbe GH, Wang H, Hase WL (1999) Adv Chem Phys 105:171–201
36. Bakken V, Millam JM, Schlegel HB (1999) J Chem Phys 111:8773–8777
37. Millam JM, Bakken V, Chen W, Hase WL, Schlegel HB (1999) J Chem Phys 111:3800–3805
38. Sousa SF, Fernandes PA, Ramos MJ (2007) J Phys Chem A 111:10439–10452
39. Lyon JT, Andews L, Malmqvist P, Roos BO, Yang T, Bursten BE (2007) Inorg Chem 46:4917–4925
40. Gagliardi L, Roos BO, Malmqvist P-Å, Dyke JM (2001) J Phys Chem A 105:10602–10606
41. Wiberg KB (1968) Tetrahedron 24:1083–1096
42. Martínez-Núñez E, Fernández-Ramos A, Cordeiro MNDS, Vázquez SA, Aoiz FJ, Bañares L (2003) J Chem Phys 119:10618–10625